Development of a Terrain Mapping/Crater Evolution Measurement using Diffractive Optical Elements

Joshua M. Weisberger*, Paul M. Danehy†, Timothy W. Fahringer‡, Brett F. Bathel§
NASA Langley Research Center, Hampton, VA, 23666

Olivia Tyrrell¶
Iowa State University, Ames, IA, 50011

When landing on the moon, understanding the interaction of the engine exhaust plume with the lunar surface is critical for the success of the descent and landing flight phases. Two evaluation tools currently used are computational simulations and ground test measurements. Computational simulations require experimental measurements for comparison/validation, but ground test measurements cannot accurately emulate all aspects of an actual lunar landing; flight tests remain the only method of obtaining fully representative data. A terrain mapping/crater evolution measurement system was developed for potential inclusion on a future lander mission. This system uses two stereo cameras viewing a laser dot grid pattern projected on the ground, where the grid is created by shining a laser through one or two diffractive optical elements. CAD simulations of the stereo imaging system are first used to validate the proposed design. Laboratory testing of the system using both a large-scale fixed-geometry crater and a small-scale evolving-geometry crater validate the use of the system for terrain mapping measurements, and for its potential inclusion on a future lander mission.

I. Introduction

For spacecraft making the journey to the moon, the entry, descent, and landing (EDL) phases of flight are critical for the mission's success. The Apollo missions provided myriad videos, images, and analysis of the descent and landing phases, and provided insight into how the engine's exhaust plume interacted with the surface of the moon [1–5]. However, many aspects of this plume-surface interaction (PSI) are still not fully described, and it is currently an active research topic in preparation for future planetary spaceflight missions. Understanding how a lunar lander engine's exhaust plume interacts with the lunar surface/regolith is important for multiple aspects of a mission. If too much lunar regolith is ejected from below the lander, the surface for the landing site could become significantly cratered and pose a tipping hazard for the lander upon touchdown (as was nearly the case in an Apollo landing). The speed and trajectories of the ejected regolith/particles from the plume can damage nearby scientific installations, existing structures, and potentially the lander itself.

Preparations for several unmanned lunar lander missions with scientific instrumentation are ongoing under the Commercial Lunar Payload Services (CLPS) initiative [6]. One of the scientific instruments is the Stereo Cameras for Lunar-Plume Surface Studies (SCALPSS), where stereo imaging of the lunar surface before, during, and after the landing will measure the crater evolution [7]. The initial iteration of this measurement system will not use structured illumination, and will obtain depth/shape maps of the lunar surface when characteristic features are visible and identifiable in both camera views.

Recent stereo imaging of crater evolution has been performed to non-intrusively measure the crater shape during a ground PSI test [8]. In this paper, a different approach is used, where a structured illumination terrain mapping and crater evolution measurement system is described. To validate the measurement technique, CAD simulations of a representative lunar lander with stereo cameras and laser grid illumination are used to produce rendered images of both undisturbed flat ground and of a typical crater below a nozzle plume (Section II). A large-scale fixed-geometry crater

*Aerospace Technologist, Advanced Measurements and Data Systems Branch, AIAA Member.
†Senior Technologist, Advanced Measurements and Data Systems Branch, AIAA Associate Fellow.
‡Aerospace Technologist, Advanced Measurements and Data Systems Branch, AIAA Member.
§Aerospace Technologist, Advanced Measurements and Data Systems Branch, AIAA Senior Member.
¶Undergraduate Student, Department of Mechanical Engineering, NASA Aeronautics Research Intern.

model is then used to test the system in the laboratory, and by using two diffractive optical elements (DOE) rotating relative to each other, the projected laser grid dot density can be changed (Section III). Finally, a small-scale PSI test is conducted to measure the changing crater shape due to a compressed air jet nozzle flow (Section IV). In this paper, specific vendor and manufacturer names are explicitly mentioned only to accurately describe the test hardware. The use of vendor and manufacturer names does not imply endorsement by the U.S. Government.

II. Computer Simulated Crater

A model of a representative lunar lander was used as the instrumentation bed for the CAD simulations, seen in a top-view render in Fig. 1a. The world coordinate system origin was located directly below the center of the lander, with the $z = 0$ position on the flat ground. In the top-view of Fig. 1b with the lander model removed, two cameras (labeled 3A and 5A) are shown positioned in their representative positions on the lander legs, and both looking at the crater centered below the main engine nozzle. Camera 3A is positioned at (−33,−28,75) inches and camera 5A is positioned at (33,−28,75) inches. Camera 3A is rotated 40° about the x-axis and −50° about the z-axis, while camera 5A is rotated 40° about the x-axis and 50° about the z-axis. The crater is seen centered below the lander, and a 19×19 laser dot grid array is positioned illuminating the crater such that the central dot always coincides with the center of the crater.

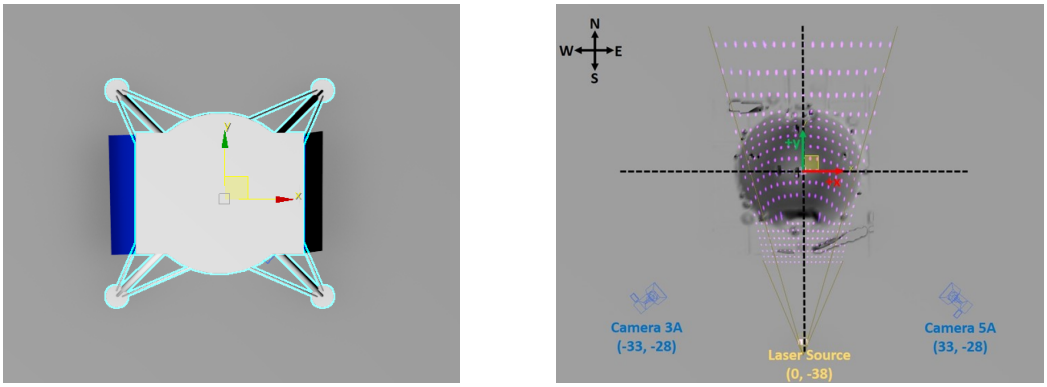

(a) **(b)**

Fig. 1 Top view of the (a) simplified lander and (b) crater, laser source/grid, and camera locations.

The intrinsic and extrinsic calibration of the cameras were computed using a rendered 8×9 checkerboard with 5 inch squares, for a total board dimension of 40×45 inches. The intrinsic calibration for each camera was computed separately, with ten images used for each calibration which provide coverage over the full camera field-of-view. For the extrinsic calibration, four image pairs were used where the checkerboard was visible in both cameras' field-of-view. The mean reproduction error for the intrinsic calibration for cameras 3A and 5A are 0.13 pixels and 0.54 pixels, respectively, and for the extrinsic calibration is 1.25 pixels. Further stereo image pair renderings are needed to lower the extrinsic calibration reproduction error.

A simulated laser grid was projected from a location equidistant between both cameras and onto the flat ground (with the crater model removed). To capture the evolution of the measurements with descent of the lander, four altitudes of the lander above the ground were simulated: 3 m, 2 m, 1 m, and 0 m (post-landing). The camera positions and views remained fixed for all altitudes, but the laser grid was repositioned for each such that the central dot was always at the world coordinate system origin (centered on the crater when included). Without this repositioning, the grid would no longer be in-view of the two cameras at higher altitudes. Renderings of the projected laser grid on the flat ground for the four altitudes are shown in Fig. 2, with corresponding camera views stacked vertically. The camera calibrations are used to rectify the two captured laser grid images, after which these rectified images are thresholded and binarized for ease of laser dot identification. The correspondence of the identified laser dots between images is established, and the disparity between these dots is computed. The camera calibrations are then again used to transform the disparity calculations back to world coordinates in three-dimensional space, allowing for a depth map of the ground (and crater) to be constructed. Since the projected laser dots have a finite diameter, the centroid of the identified dot is used for the calculations. The depth maps for each altitude are shown below their corresponding renderings in Fig. 2, where the

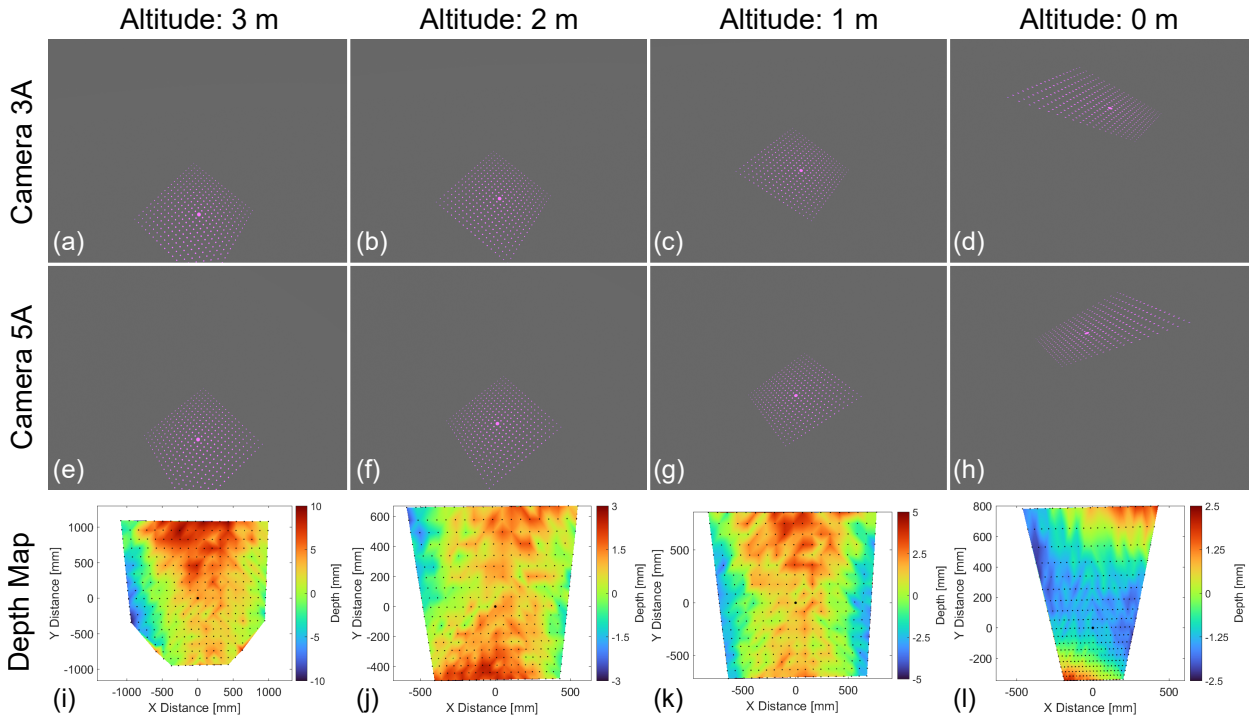

Fig. 2 Flat ground renderings with projected laser grid, with images from (a-d) camera 3A and (e-h) camera 5A, and corresponding depth maps for lander altitudes of (a,e,i) 3 m**, (b,f,j)** 2 m**, (c,g,k)** 1 m**, and (d,h,l)** 0 m**.**

laser dots are identified with black dots and the central dot is largest. Even with the laser grid repositioned at an altitude of 3 m, some of the corner dots were cut off in each camera view and could not be used to compute the depth at those positions (dots must be visible in both cameras for a depth measurement). Note that the colorbar scale is different for each depth map. For true flat ground measurements, the depth should be 0 mm, but for higher altitudes the ± depth error increases.

The crater model was then included in the CAD simulations in place of the original flat ground. The data for the crater was taken from measurements of a spherical-cap shaped sled using a photogrammetric system. The camera positions/orientations continued to remain fixed, and the crater model, once placed in its position on the ground, also remained fixed. As the altitude of the lander was changed, the laser grid was angled such that its central dot was located at the center of the crater. Renderings of the projected laser grid on the crater for the four altitudes are shown in Fig. 3, with corresponding camera views stacked vertically. The depth map calculations were the same as the flat ground calculations. These resulting depth maps in Fig. 3 all have the same colorbar limits, from the undisturbed flat ground outside the crater at 0 mm, to the maximum crater depth at approximately −110 mm. The measured crater shape remains roughly the same for all altitudes, and compares favorably to the coordinates of the model itself. At the highest altitude of 3 m, only approximately 40 laser dots are included in the crater extents, while when the lander is on the ground at 0 m, more than four times as many laser dots are used to measure the crater shape. This motivates the need for different DOE projected grids, or potentially an adjustable system, as described in Section III.

III. Large-Scale Fixed-Geometry Crater Model

A large 6×6 foot fixed-geometry crater model was used for laboratory testing of the stereo imaging system, and was designed to have an asymmetrical outline of approximately 1200 mm with a depth of approximately 50 mm to 75 mm. The crater model was constructed using a 2×4 backing structure with chicken wire and two to three layers of paper maché to define the fine surface structure. The top layer of paper maché was painted with a thick layer of grey latex paint and dusted with a concrete mixture to add texture and approximate the uniform color of the regolith. Intermittent rocks were spread over the surface to provide larger-scale features characteristic of the lunar surface. The

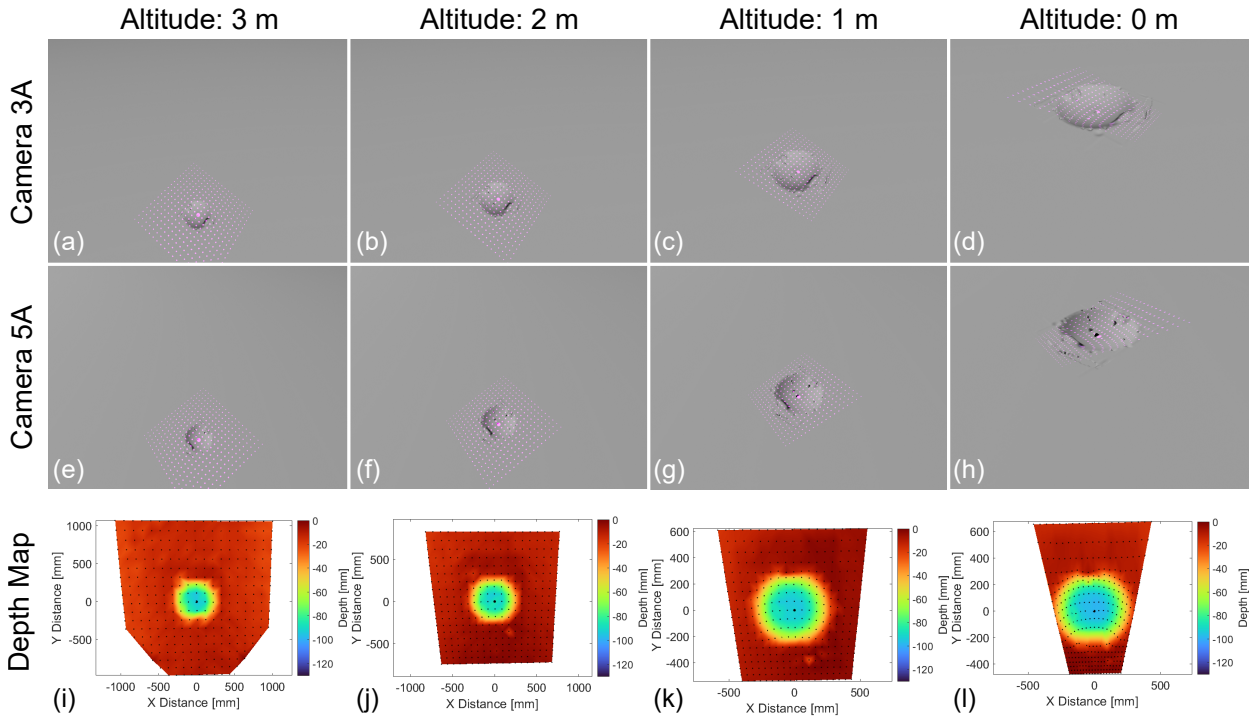

Fig. 3 Crater renderings with projected laser grid, with images from (a-d) camera 3A and (e-h) camera 5A, and corresponding depth maps for lander altitudes of (a,e,i) 3 m**, (b,f,j)** 2 m**, (c,g,k)** 1 m**, and (d,h,l)** 0 m**.**

exact geometry of the crater model was measured using an industrial photogrammetric system (V-STARS, Geodetic Systems, Inc.) to provide a ground-truth for comparison. The use of the PRO-Spot dot projection with this system allows for measurements up to approximately 4 μm with 1 cm spatial resolution. To increase the resolution of the data set, four separate slight overlapping regions of the crater were independently measured and then stitched together in Autodesk 3DS Max.

Two FLIR Chameleon3 USB3 cameras (CM3-U3-13Y3C-S-BD) with 3.37 mm focal length lenses (PeauProduction) were used to image the crater. The cameras were mounted to an optical table with approximately 1085 mm separation. The laser and DOE were mounted approximately centered between the two cameras as it was in the CAD simulations. The laser grid was shined on the crater model surface, and the cameras were angled such that the central laser dot was approximately centered on both fields-of-view. The left and right cameras were approximately 1345 mm and 1420 mm from the central dot on the crater. A red laser pointer with two rotatable plastic DOEs provided a bright, adjustable laser grid pattern. Six different patterns capable of being produced with this adjustable laser/DOE combination are shown in Fig. 4 (imaged by the right camera). The grids in (a), (c), and (d) are used to compute depth maps seen later in Fig. 5. The brighter central dot provided a known anchoring point between cameras, which is useful when it would otherwise be hard to determine dot connectivity between the images with a large number of dots in a regular pattern.

A large 8×7 checkerboard calibration target was used for both the intrinsic and extrinsic camera calibrations, using 4.75 inch squares for a total board size of 38×33.25 inches. Each camera's intrinsic calibration was computed separately, after which an extrinsic stereo calibration was computed using different images visible to both cameras simultaneously. For the left camera, 84 images were used for the intrinsic calibration, with a resulting mean reproduction error of 0.15 pixels, while for the right camera, 61 images were used with a resulting mean reproduction error of 0.14 pixels. For the extrinsic calibration, 2 image pairs were used with a resulting mean reproduction error of 0.52 pixels.

Depth maps are computed for the crater model using three of the laser grid densities/configurations shown in Fig. 4. Depth maps corresponding to Figs. 4(a,c,d) are shown in Figs. 5(a,b,c), respectively. The maps show a top-view of the crater (viewing the x-y plane), where the small black dots are the laser grid dots that are visible in both stereo camera views, and are thus used for the calculations. All colorbar limits are the same, from 0 mm (flat ground) to -80 mm (deepest part of the crater model). With the increasing laser grid density, the crater shape becomes more defined, and rocks can also be identified when a laser dot happens to coincide with one (much less likely for coarser grids). In Fig.

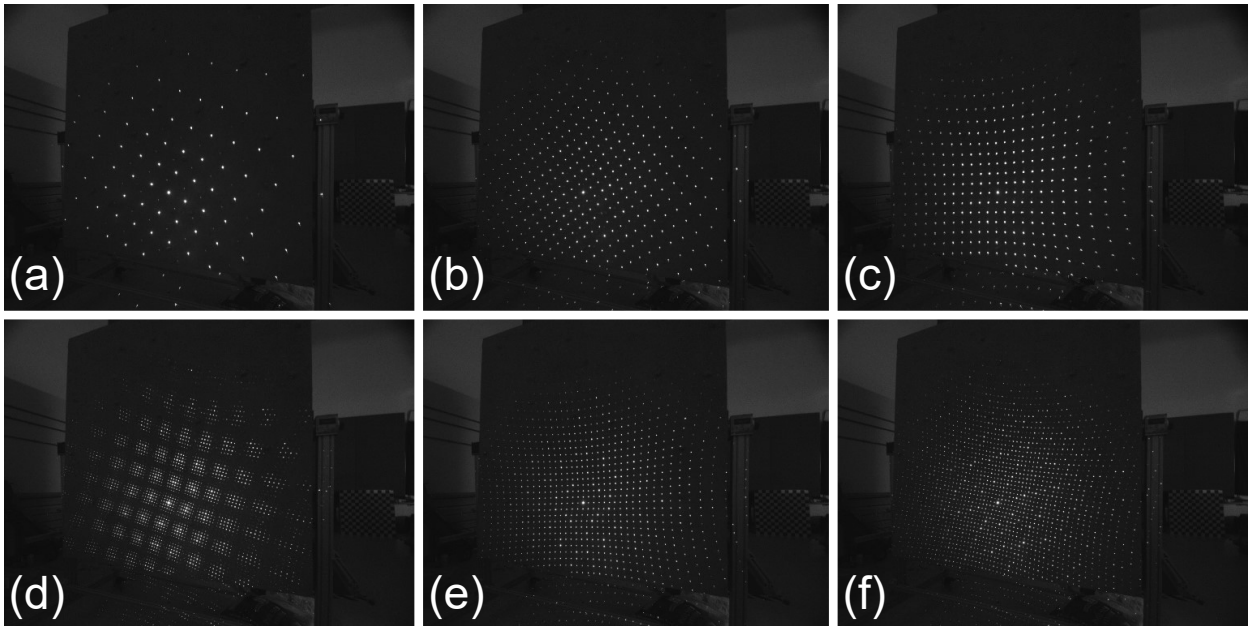

Fig. 4 Six different projected grid patterns produced by rotating two diffractive optical elements relative to one another in front of a laser beam. Resulting depth maps from (a,c,d) are shown in Fig. 5.

5(d), the ground-truth elevation map is shown, and is scaled to roughly the same size as the depth maps. The bulk computed crater shape compares favorably to this ground-truth, and identified rocks in the depth maps of (b) and (c) are shown with appropriately oriented arrows.

IV. Plume-Surface Interaction Crater Evolution

A small-scale enclosure was constructed to acquire image sequences during a plume-surface interaction test using compressed air exhausted through a small nozzle, and impinging on a bed of particles. The enclosure shown in Fig. 6 is constructed with three acrylic side windows for optical access, a removable rear panel for calibration, cleanup, and resetting, and a top panel with two acrylic window inserts for the stereo camera optical access. The nozzle passes through the center of the top panel, and is connected to the laboratory compressed air bottle through a flow meter for air pressure adjustments. The 254 μm silicon carbide lapping grain particles (McMaster-Carr, 4780A36) are placed in a tray resting on the floor of the enclosure. Prior to a test, the particles are moved to the center of the tray and are flattened to provide an initial level ground.

Two identical machine vision cameras (Basler, acA1920-150um) with 25 mm focal length lenses (Tamron) are placed on top of the enclosure, each viewing the particle bed below the nozzle through their respective acrylic window viewing ports. A low power (0.9 mW) 520 nm USB laser (Thorlabs, PL201) with a 3 mm diameter beam was projected through a diffractive optical element (Holoeye, DER-243) to produce a 17×17 laser grid. The central dot of the resulting projected grid is brighter than the rest, making it a useful marker for identifying matching grid points in both camera images. While the DOE was constructed for lasers operating at 633 nm, the green laser provided a smaller angular deviation, resulting in a tighter projected grid, with more dots defining the crater than a red laser would provide. A blue laser was also available for an even smaller angular deviation, but the intensity of the light projected onto the particle bed was too low to be used. The laser grid was shined onto the particle bed from the side window of the enclosure (opposite the removed panel, see Fig. 6(a)). The bright central dot was placed directly below the nozzle, centering the grid on the flat ground. Due to the angle of the laser grid from the side window, as the crater deepens during a test, the central dot will no longer be centered below the nozzle. This does not pose a problem however, and the central dot placement is simply used to align both cameras prior to the test to ensure maximum field-of-view coverage of the eventual crater.

The cameras were pointed at the central dot of the grid on the flat ground, and the aperture ring and focus ring locked in place. The enclosure lid (with cameras attached) was lifted off the enclosure and placed on the optical table to

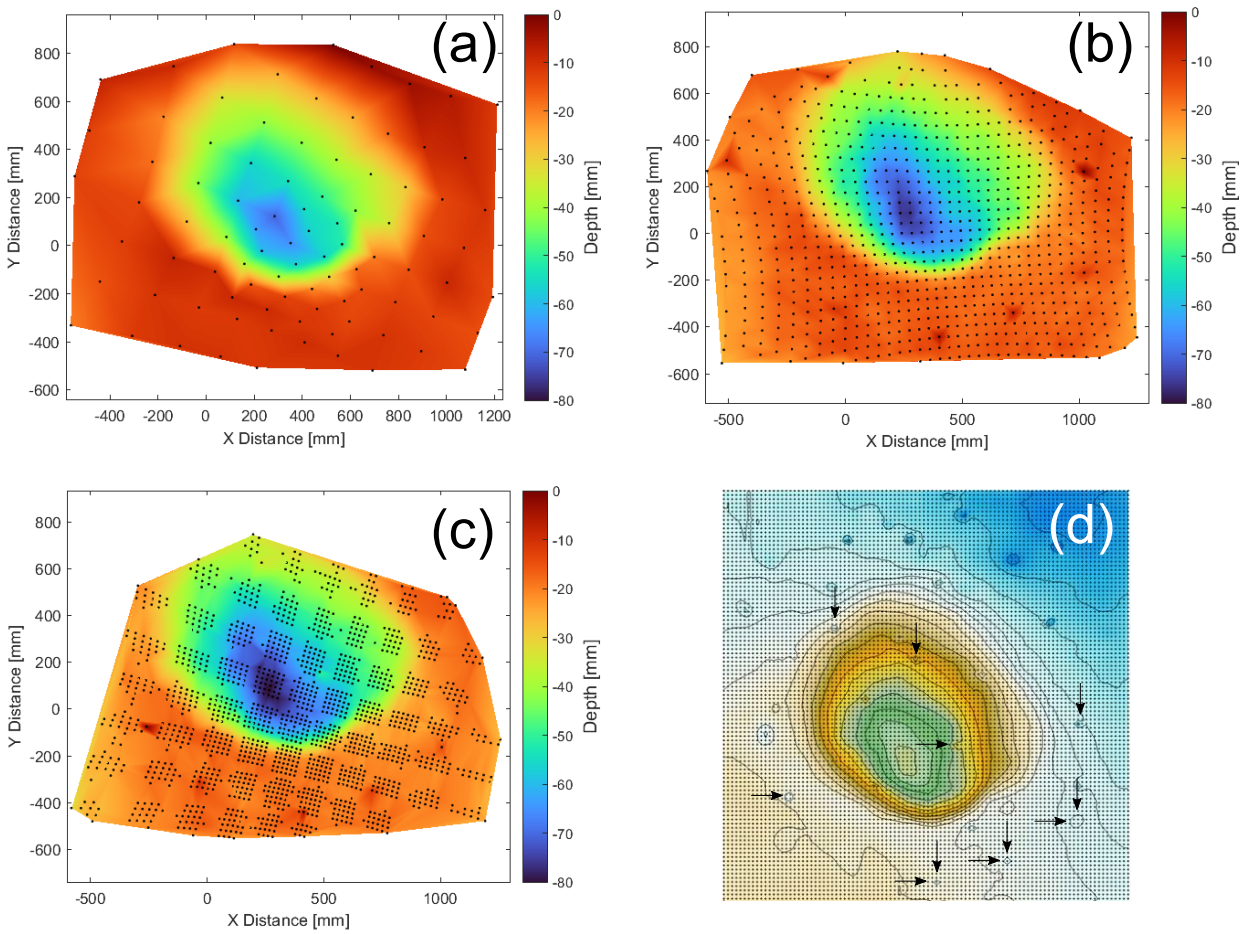

Fig. 5 Crater model laser/DOE reconstructed depth maps for (a) least dense dot pattern, (b) medium density dot pattern, and (c) highest density dot patter, along with the (d) V-STARS crater model data as the ground-truth. Black arrows in (d) show identified rocks crater reconstructions (b) and (c), respective to arrow direction.

perform the calibrations, since space was limited inside the enclosure to get the necessary views of the calibration target. A smaller 9×8 checkerboard calibration target was used due to the smaller field-of-view of the measurements inside the enclosure. The size of the squares was 7 mm for a total calibration target size of 63×54 mm. For the left camera, 127 images were used for the intrinsic calibration, with a resulting mean reproduction error of 0.89 pixels, while for the right camera, 121 images were used with a resulting mean reproduction error of 0.94 pixels. For the extrinsic calibration, 25 image pairs were used with a resulting mean reproduction error of 0.99 pixels. After calibration, the lid was carefully placed back on top of the enclosure for testing.

Images from the left camera during a PSI test are shown in Fig. 7. Frames (a-e) are sequential, with frame (a) taken just before the nozzle flow is turned on. Frame (f) is taken after the nozzle flow has been turned off after the test, showing the final crater shape. The computed depth maps are shown below their respective camera images, where the colorbar limits are the same for (a-e), but is different for (f). With each successive frame, the crater shape evolves and deepens. The resolution of the laser grid is fairly coarse, but the general circular shape can be inferred. For the post-test crater depth map, the circular shape and depth of the final crater is more evident, although due to the angle of incidence of the laser relative to the crater, there is an absence of grid points on the near (bottom) edge of the crater. This can be remedied by introducing the laser from above instead, or by using to different laser/DOE units at complementary positions to obtain full coverage over all expected crater geometries.

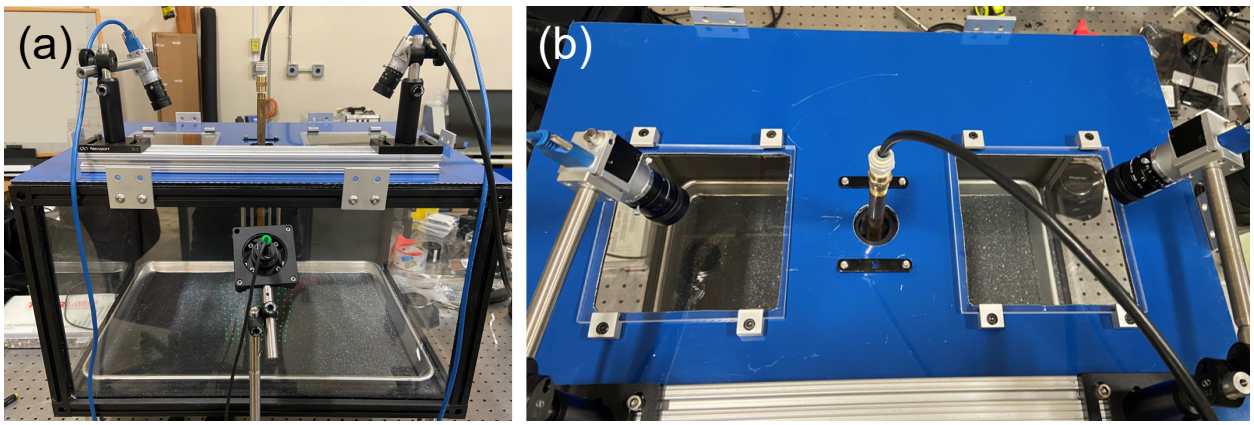

Fig. 6 Plume-surface interaction enclosure (a) side view and (b) top view.

Acknowledgments

This work was supported by the NASA CIF/IRAD program under the FY21 project titled "Particle Image Velocimetry/Tracking, Ejecta Sheet Monitoring, and Terrain Mapping for SCALPSS 2". The authors thank William Hutchins and Ryan Thompson for the fabrication and photogrammetric measurements of the large fixed-geometry crater model, as well as Stephen Jones and Holt Ripley for the fabrication of the small-scale PSI enclosure.

References

[1] Engle, M., "Operational Considerations for Manned Lunar Landing Missions - Lessons Learned from Apollo," *AIAA Space 2004 Conference and Exhibit*, American Institute of Aeronautics and Astronautics, 2004. doi:10.2514/6.2004-6081.

[2] Gaier, J. R., "The Effects of Lunar Dust on EVA Systems During the Apollo Missions," techreport 2005-213610, NASA Glenn Research Center, Mar. 2005. URL `https://history.nasa.gov/alsj/TM-2005-213610.pdf`.

[3] Metzger, P. T., Lane, J. E., Immer, C. D., and Clements, S., "Cratering and Blowing Soil by Rocket Engines During Lunar Landings," *International Conference on Case Histories in Geotechnical Engineering*, 2008. URL `https://scholarsmine.mst.edu/cgi/viewcontent.cgi?article=2931&context=icchge`.

[4] Metzger, P. T., Smith, J., and Lane, J. E., "Phenomenology of soil erosion due to rocket exhaust on the Moon and the Mauna Kea lunar test site," *Journal of Geophysical Research*, Vol. 116, No. E6, 2011. doi:10.1029/2010je003745.

[5] Jones, E. M., and Glover, K., "Apollo Lunar Surface Journal," Online, Nov. 2017. URL `https://www.hq.nasa.gov/alsj/main.html`, https://www.hq.nasa.gov/alsj/main.html.

[6] Dunbar, B., "https://www.nasa.gov/content/commercial-lunar-payload-services-overview," Online, Jun. 2021.

[7] Thompson, R. J., Danehy, P. M., Munk, M. M., Mehta, M., Manginelli, M. S., Nguyen, C., and Thomas, O. H., "Stereo Camera Simulation for Lunar Surface Photogrammetry," *AIAA SciTech 2021*, American Institute of Aeronautics and Astronautics, 2021. doi:10.2514/6.2021-0358.

[8] Stubbs, D., Silwal, L., Thurow, B. S., Hirabayashi, M., Raghav, V., and Scarborough, D., "Non-intrusive, 3D Optical Measurements of Crater Formation due to Plume-Surface Interactions," *AIAA SciTech 2021 Forum*, American Institute of Aeronautics and Astronautics, 2021. doi:10.2514/6.2021-0831.

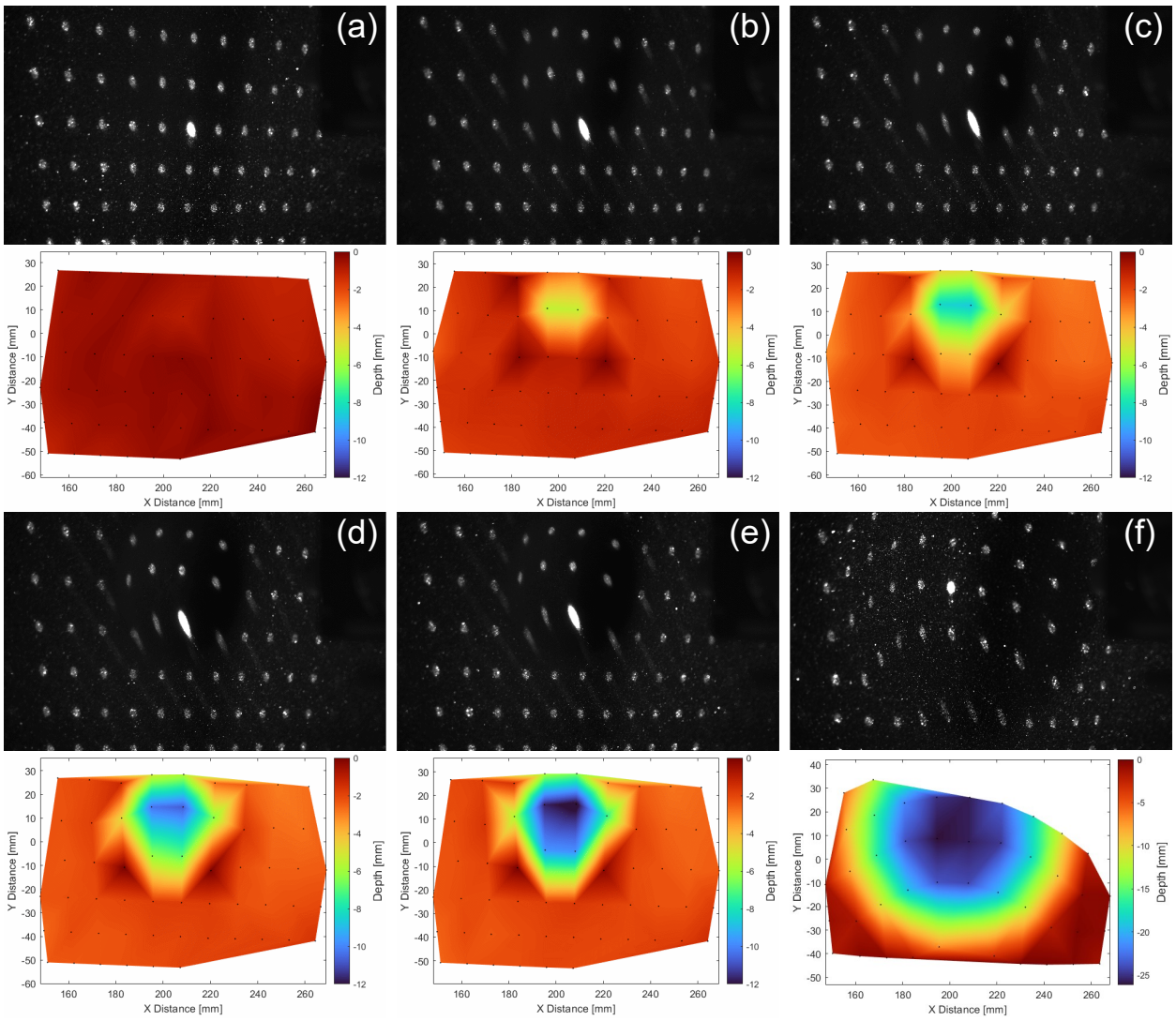

Fig. 7 Left camera image sequence and computed stereo depth maps for the small-scale plume-surface interaction testing. Images (a-e) are the first five frames of the test, whereas (f) is the post-test crater image. Colorbar limits are the same for (a-e) at [0 mm,−12 mm**], but is different for (f) at [**0 mm,−25 mm**].**